

1

## 2      The ANTsX Ecosystem for Spatiotemporal 3      Mapping of the Mouse Brain

4      Nicholas J. Tustison<sup>1</sup>, Min Chen<sup>2</sup>, Fae N. Kronman<sup>3</sup>, Jeffrey T. Duda<sup>2</sup>, Clare Gamlin<sup>4</sup>,  
5      Lydia Ng<sup>4</sup>, Yongsoo Kim<sup>3</sup>, and James C. Gee<sup>2</sup>

6      <sup>1</sup>Department of Radiology and Medical Imaging, University of Virginia, Charlottesville, VA

7      <sup>2</sup>Department of Radiology, University of Pennsylvania, Philadelphia, PA

8      <sup>3</sup>Department of Neural and Behavioral Sciences, Penn State University, Hershey, PA

9      <sup>4</sup>Allen Institute for Brain Science, Seattle, WA

10

---

11      Corresponding author:

12      Nicholas J. Tustison, DSc

13      Department of Radiology and Medical Imaging

14      University of Virginia

15      [ntustison@virginia.edu](mailto:ntustison@virginia.edu)

<sub>16</sub> **Abstract**

<sub>17</sub> Precision mapping techniques coupled with high resolution image acquisition of the mouse  
<sub>18</sub> brain permit the study of the spatial organization of gene activity and their mutual interac-  
<sub>19</sub> tion for a comprehensive view of salient structural/functional relationships. Such research  
<sub>20</sub> is facilitated by standardized anatomical coordinate systems, such as the well-known Allen  
<sub>21</sub> Common Coordinate Framework version 3 (CCFv3), and the ability to map to such refer-  
<sub>22</sub> ence atlases. The Advanced Normalization Tools Ecosystem (ANTsX) is a comprehensive  
<sub>23</sub> open-source software image analysis toolkit with applicability to multiple organ systems,  
<sub>24</sub> modalities, and animal species. Herein, we illustrate the utility of ANTsX for generating  
<sub>25</sub> precision spatial mappings of the mouse brain of different developmental ages including the  
<sub>26</sub> prerequisite preprocessing steps. Additionally, as a further illustration of ANTsX capabil-  
<sub>27</sub> ities, we use these publicly available mouse brain atlases to generate a velocity flow-based  
<sub>28</sub> mapping encompassing the entire developmental trajectory, which we also make available to  
<sub>29</sub> the public.

## <sup>30</sup> Introduction

<sup>31</sup> Over the past two decades there has been a notable increase in significant advancements in  
<sup>32</sup> mesoscopic analysis of the mouse brain. It is now possible to track single cell neurons in 3-D  
<sup>33</sup> across full mouse brains,<sup>1</sup> observe whole brain developmental changes on a cellular level,<sup>2</sup>  
<sup>34</sup> associate brain regions and tissues with their genetic composition,<sup>3</sup> and locally characterize  
<sup>35</sup> neural connectivity.<sup>4</sup> Much of this scientific achievement has been made possible due to  
<sup>36</sup> breakthroughs in high resolution imaging techniques that permit submicron, 3-D imaging  
<sup>37</sup> of whole mouse brains. Associated research techniques such as micro-optical sectioning  
<sup>38</sup> tomography,<sup>6</sup> tissue clearing,<sup>1,7</sup> spatial transcriptomics<sup>9</sup> are all well-utilized in the course of  
<sup>39</sup> scientific investigations of mesoscale relationships in the mouse brain.

<sup>40</sup> An important component of these research programs is the ability to map the various image  
<sup>41</sup> data to anatomical reference frames<sup>11</sup> for inferring spatial relationships between structures,  
<sup>42</sup> cells, and genetics in the brain. This has motivated the development of detailed struc-  
<sup>43</sup> tural image atlases of the mouse brain. Notable examples include the Allen Brain Atlas  
<sup>44</sup> and Coordinate Frameworks<sup>13</sup> and the Waxholm Space.<sup>14</sup> Despite the significance of these  
<sup>45</sup> contributions, challenges still exist in large part due to the wide heterogeneity in associ-  
<sup>46</sup> ated study-specific image data. Variance in the acquisition methods can introduce artifacts  
<sup>47</sup> such as tissue distortion, holes, bubbles, folding, tears, and missing slices. These severely  
<sup>48</sup> complicate assumed correspondence for registration.

<sup>49</sup> To address such challenges, several software packages have been developed over the years  
<sup>50</sup> comprising solutions of varying comprehensibility, sophistication, and availability. An early  
<sup>51</sup> contribution to the community was the Rapid Automatic Tissue Segmentation (RATS)  
<sup>52</sup> package<sup>15</sup> for brain extraction (available upon request). Of the publicly available pack-  
<sup>53</sup> ages, most, if not all rely on well-established package dependencies originally developed on  
<sup>54</sup> human brain data. Another early tool was SPMMouse<sup>16</sup> based on the well-known Statistical  
<sup>55</sup> Parametric Mapping (SPM) software package.<sup>17</sup> The automated mouse atlas propagation  
<sup>56</sup> (aMAP) tool is largely a front-end for the NiftyReg image registration package<sup>18</sup> applied  
<sup>57</sup> to mouse data which is currently available as a Python module.<sup>19</sup> NiftyReg is also used by  
<sup>58</sup> the Atlas-based Imaging Data Analysis (AIDA) MRI pipeline<sup>20</sup> as well as the Multi Atlas

59 Segmentation and Morphometric Analysis Toolkit (MASMAT). Whereas the former also in-  
60 corporates the FMRIB Software Library (FSL)<sup>21</sup> for brain extraction and DSISTudio<sup>22</sup> for  
61 DTI processing, the latter uses NiftySeg and multi-consensus labeling tools<sup>23</sup> for brain extrac-  
62 tion and parcellation. In addition, MASMAT incorporates N4 bias field correction<sup>24</sup> from the  
63 Advanced Normalization Tools Ecosystem (ANTsX)<sup>25</sup> as do the packages Multi-modal Image  
64 Registration And Connectivity anaLysis (MIRACL),<sup>26</sup> Saamba-MRI,<sup>27</sup> and Small Animal  
65 Magnetic Resonance Imaging (SAMRI).<sup>28</sup> However, whereas Saamba-MRI uses AFNI<sup>29</sup> for  
66 image registration; MIRACL, SAMRI, and BrainsMap<sup>30</sup> all use ANTsX tools for comput-  
67 ing image-based correspondences. Other packages use landmark-based approaches to image  
68 registration including SMART—<sup>31</sup>an R package for semi-automated landmark-based regis-  
69 tration and segmentation of mouse brain based on WholeBrain.<sup>32</sup> FriendlyClearMap<sup>33</sup> uses  
70 the landmark-based registration functionality of Elastix.<sup>34</sup> Finally, the widespread adop-  
71 tion of deep learning techniques has also influenced development in mouse brain imaging  
72 methodologies. For example, if tissue deformations are not considered problematic for a  
73 particular dataset, DeepSlice can be used to determine affine mappings<sup>35</sup> with the optimal  
74 computational efficiency associated with neural networks.

## 75 The ANTsX Ecosystem

76 As noted above, many of the existing approaches for processing of mouse brain image data  
77 use ANTsX tools for core steps in various workflows, particularly its pairwise, intensity-  
78 based image registration tools and bias field correction. Historically, ANTsX development  
79 is originally based on fundamental approaches to image mapping,<sup>36–38</sup> particularly in the  
80 human brain, which has resulted in core contributions to the field such as the well-known and  
81 highly-vetted Symmetric Normalization (SyN) algorithm.<sup>39</sup> Since its development, various  
82 independent platforms have been used to evaluate ANTsX image registration capabilities in  
83 the context of different application foci which include multi-site brain MRI data,<sup>40</sup> pulmonary  
84 CT data,<sup>41</sup> and most recently multi-modal brain registration in the presence of tumors.<sup>42</sup>  
85 Apart from its registration capabilities, ANTsX is a comprehensive biological and medical  
86 image analysis toolkit, that comprises additional functionality such as template generation,

Table 1: Sampling of ANTsX functionality

<i>ANTsPy: Preprocessing</i>	
bias field correction	<code>n4_bias_field_correction(...)</code>
image denoising	<code>denoise_image(...)</code>
<i>ANTsPy: Registration</i>	
image registration	<code>registration(...)</code>
template generation	<code>build_template(...)</code>
landmark registration	<code>fit_transform_to_paired_points(...)</code>
time-varying landmark reg.	<code>fit_time_varying_transform_to_point_sets(...)</code>
integrate velocity field	<code>integrate_velocity_field(...)</code>
invert displacement field	<code>invert_displacement_field(...)</code>
<i>ANTsPy: Segmentation</i>	
General segmentation	<code>atropos(...)</code>
Joint label fusion	<code>joint_label_fusion(...)</code>
diffeomorphic thickness	<code>kelly_kapowski(...)</code>
<i>ANTsPy: Miscellaneous</i>	
Regional intensity statistics	<code>label_stats(...)</code>
Regional shape measures	<code>label_geometry_measures(...)</code>
B-spline approximation	<code>fit_bspline_object_to_scattered_data(...)</code>
Visualize images and overlays	<code>plot(...)</code>
<i>ANTsPyNet</i>	
brain extraction	<code>mouse_brain_extraction(...modality="t2"...)</code> <code>mouse_brain_extraction(...modality="ex5"...)</code>
foreground extraction	<code>mouse_histology_brain_mask(...)</code>
midline segmentation	<code>mouse_histology_hemispherical_coronal_mask(...)</code>
cerebellum segmentation	<code>mouse_histology_cerebellum_mask(...)</code>
super resolution	<code>mouse_histology_super_resolution(...)</code>

ANTsX provides state-of-the-art open-science functionality for processing image data. Such tools, including deep learning networks, support a variety of mapping-related tasks. A more comprehensive listing of ANTsX tools with self-contained R and Python examples is provided as a gist page on GitHub (<https://tinyurl.com/antsxtutorial>).

general data approximation, and deep learning networks specifically trained for mouse data (see Table 1). The collective use of the toolkit has demonstrated superb performance in multiple application areas (e.g., consensus labeling,<sup>43</sup> brain tumor segmentation,<sup>44</sup> and cardiac motion estimation).<sup>45</sup> Importantly, ANTs is built on the Insight Toolkit (ITK)<sup>46</sup> deriving benefit from a very capable open-source community of scientists and programmers as well as providing a visible, open-source venue for algorithmic contributions.

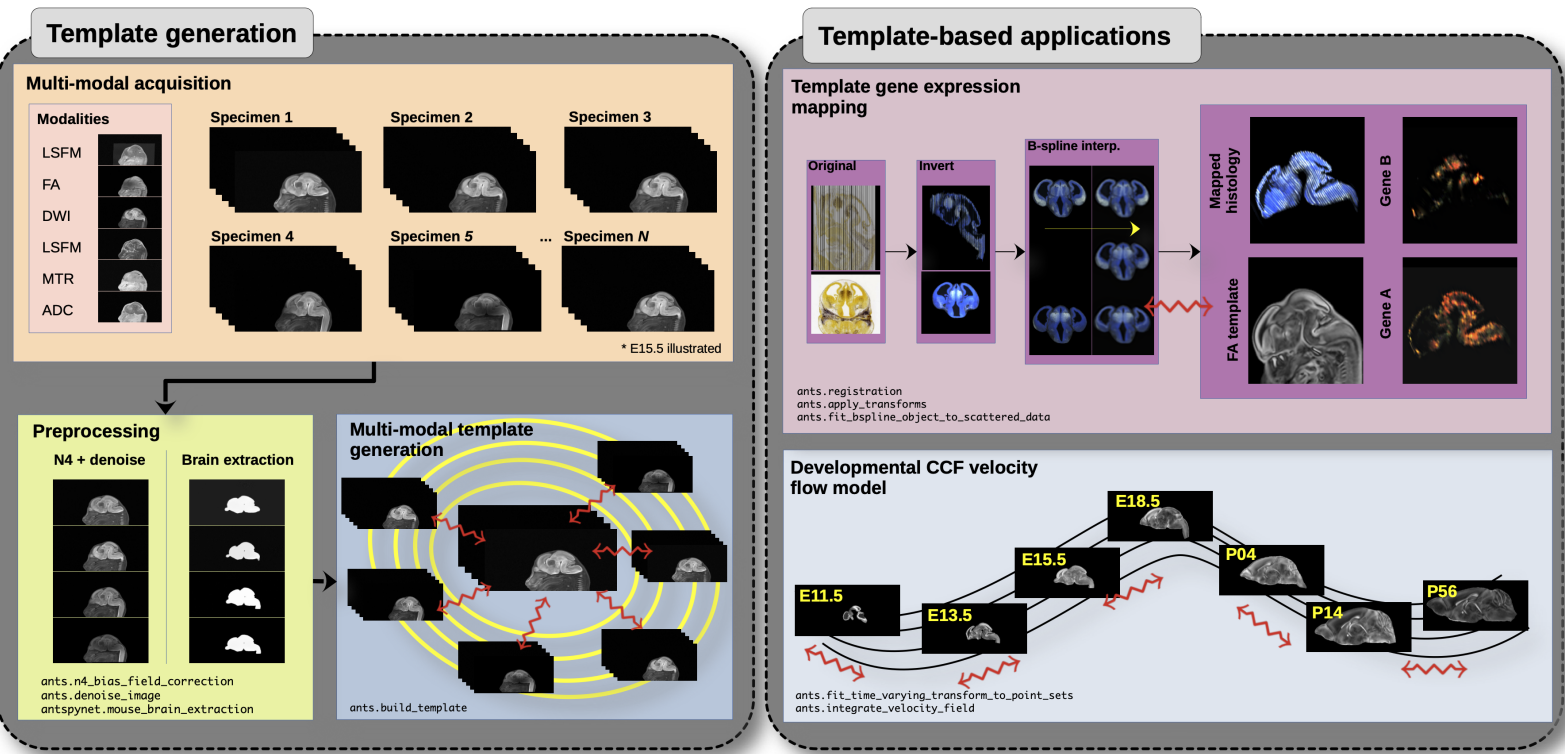


Figure 1: Illustration of a mouse brain template generation workflow and related template-based applications demonstrating the utility of different ANTsX tools. After imaging acquisition of the study population, various preprocessing steps are applied to the imaging data such as bias correction, denoising, and brain extraction as dictated by the needs of the study protocol. Not shown is the possibility of template symmetrization by contralaterally flipping the image data associated with each specimen. In the case of the DevCCF, applications include gene expression mapping and the associated velocity flow model for pseudo-template generation.

Recently, the developmental common coordinate framework (DevCCF) was introduced to the mouse brain research community as a public resource.<sup>47</sup> These symmetric atlases, comprising both multimodal image data and anatomical segmentations defined by developmental

96 ontology, span the mouse embryonic days (E) 11.5, E13.5, E15.5, E18.5 and postnatal day  
97 (P) 4, P14, and P56. Modalities include at least four MRI contrasts and light sheet flores-  
98 cence microscopy (LSFM) per developmental stage. Gene expression and other cell type  
99 data were mapped to the corresponding developmental time point to guide the associated  
100 anatomical parcellations. To further demonstrate the practical utility of the DevCCF, the  
101 P56 template was integrated with the Allen CCFv3 for mapping spatial transcriptome cell-  
102 type data. These processes, specifically template generation and multi-modal image map-  
103 ping, were performed using ANTsX functionality in the presence of previously noted image  
104 mapping difficulties (e.g., missing slices, tissue distortion) illustrated in Figure 1.

105 Given the temporal gaps in the discrete set of developmental atlases, we augment the tem-  
106 plate generation explanation previously given<sup>47</sup> from a developer’s perspective. We hope that  
107 this will provide additional information for the interested reader for potential future template  
108 generation. Related, we also provide a complementary strategy for inferring correspondence  
109 and mapping information within the temporally continuous domain spanned and sampled by  
110 the existing set of embryonic and postnatal atlas brains of the DevCCF. Recently developed  
111 ANTsX functionality include the generation of a diffeomorphic velocity flow transformation  
112 model<sup>48</sup> spanning developmental stages where mappings between any two continuous time  
113 points within the span bounded by the E11.5 and P56 atlases is determined by integration  
114 of the generated time-varying velocity field.<sup>49</sup> Such transformations permit the possibility of  
115 “pseudo” templates generated between available developmental stages.

<sub>116</sub> **Results**

<sub>117</sub> **Template building**

<sub>118</sub> Template building using ANTsX tools was first described in.<sup>50</sup> Subsequently, multi-modal and  
<sub>119</sub> symmetrical variants were more explicitly described as part of the brain tumor segmentation  
<sub>120</sub> approach.<sup>51</sup>

<sub>121</sub> **The DevCCF Velocity Flow Model**

<sub>122</sub> To continuously link the DevCCF atlases, a velocity flow model was constructed using Dev-  
<sub>123</sub> CCF derived data and ANTsX functionality available in both ANTsR and ANTsPy. Al-  
<sub>124</sub> though many implementations optimize variations of this transformation model (and others)  
<sub>125</sub> using various image intensity similarity metrics, we opted to implement a separate de-  
<sub>126</sub> termination of iterative correspondence and transformation optimization. This decision was  
<sub>127</sub> based on existing ANTsX functionality and wanting complementary utility for the toolkit.

<sub>128</sub> ANTsX, being built on top of ITK, uses an ITK image data structure for the 4-D velocity  
<sub>129</sub> field where each voxel contains the  $x$ ,  $y$ ,  $z$  components of the field at that point. Field  
<sub>130</sub> regularization is provided by a novel B-spline scattered data approximation technique<sup>52</sup> which  
<sub>131</sub> permits individual point-based weighting. Both field regularization and integration of the  
<sub>132</sub> velocity field are built on ITK functions written by ANTsX developers.

<sub>133</sub> The optimized velocity field described here is of size [256, 182, 360] (or  $50\mu\text{m}$  isotropic)  $\times 11$   
<sub>134</sub> integration points for a total compressed size of a little over 2 GB. This choice represented  
<sub>135</sub> weighing the trade-off between tractability, portability, and accuracy. However, all data  
<sub>136</sub> and code to reproduce the results described are available in a dedicated GitHub repository  
<sub>137</sub> (<https://github.com/ntustison/DevCCF-Velocity-Flow>).

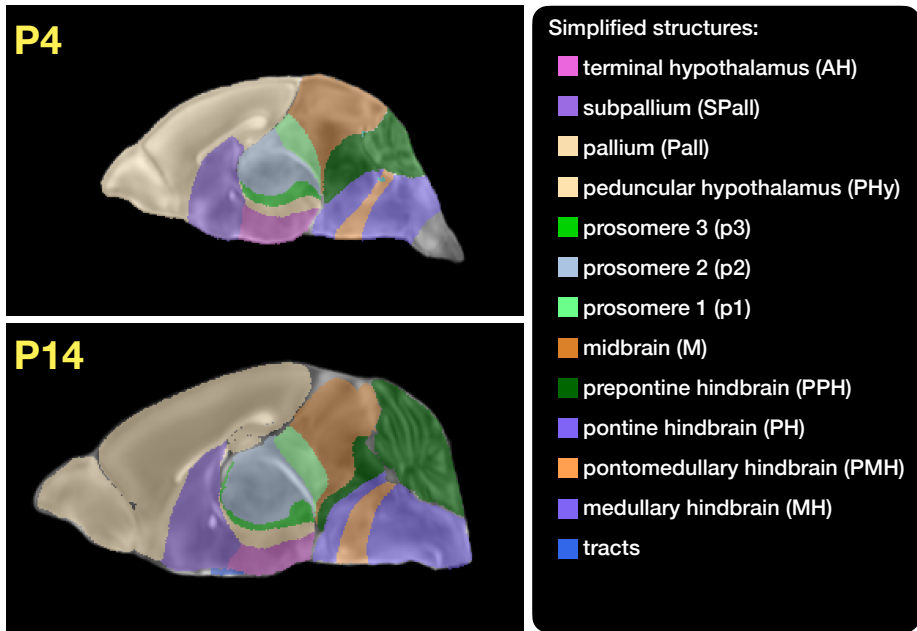


Figure 2: Annotated regions representing common labels across developmental stages which are illustrated for both P4 and P14.

### <sup>138</sup> Data preparation

<sup>139</sup> Labeled annotations are available as part of the original DevCCF and reside in the space  
<sup>140</sup> of each developmental template which range in resolution from  $31.5 - 50\mu\text{m}$ . Across all atlases,  
<sup>141</sup> the total number of labels exceeded 2500 without taken into account per hemispherical  
<sup>142</sup> enumeration. From this set of labels, there were a common set of 24 labels (12 per hemisphere)  
<sup>143</sup> across all atlases that were used for optimization and evaluation. These regions are  
<sup>144</sup> illustrated for the P4 and P14 stages in Figure 2.

<sup>145</sup> Prior to velocity field optimization, the data was rigidly transformed to a common  
<sup>146</sup> space. Using the centroids for the common label set of each CCFDev atlas, the ANTsPy  
<sup>147</sup> `ants.fit_transform_to_paired_points(...)` function was used to warp each atlas  
<sup>148</sup> to the space of the P56 atlas and then downsampled to  $50\mu\text{m}$  isotropic resolution. In  
<sup>149</sup> order to determine the common point sets across stages, the multi-metric capabilities  
<sup>150</sup> of `ants.registration(...)` were used. Instead of performing intensity-based pairwise  
<sup>151</sup> registration directly on these multi-label images, each label was used to construct a separate  
<sup>152</sup> fixed and moving image pair resulting in a multi-metric registration optimization scenario

153 involving 24 binary image pairs (each label weighted equally) for optimizing correspondence  
154 between neighboring atlases using the mean squares metric and the SyN transform.

155 To provide the common point sets across all seven developmental atlases, the label boundaries  
156 and whole regions were sampled in the P56 atlas (10% for the former and 1% for the latter)  
157 and then propagated to each atlas using the transformations derived from the pairwise  
158 registrations. Boundary points were weighted twice as those of regional points in the B-  
159 spline optimization.

## 160 Optimization

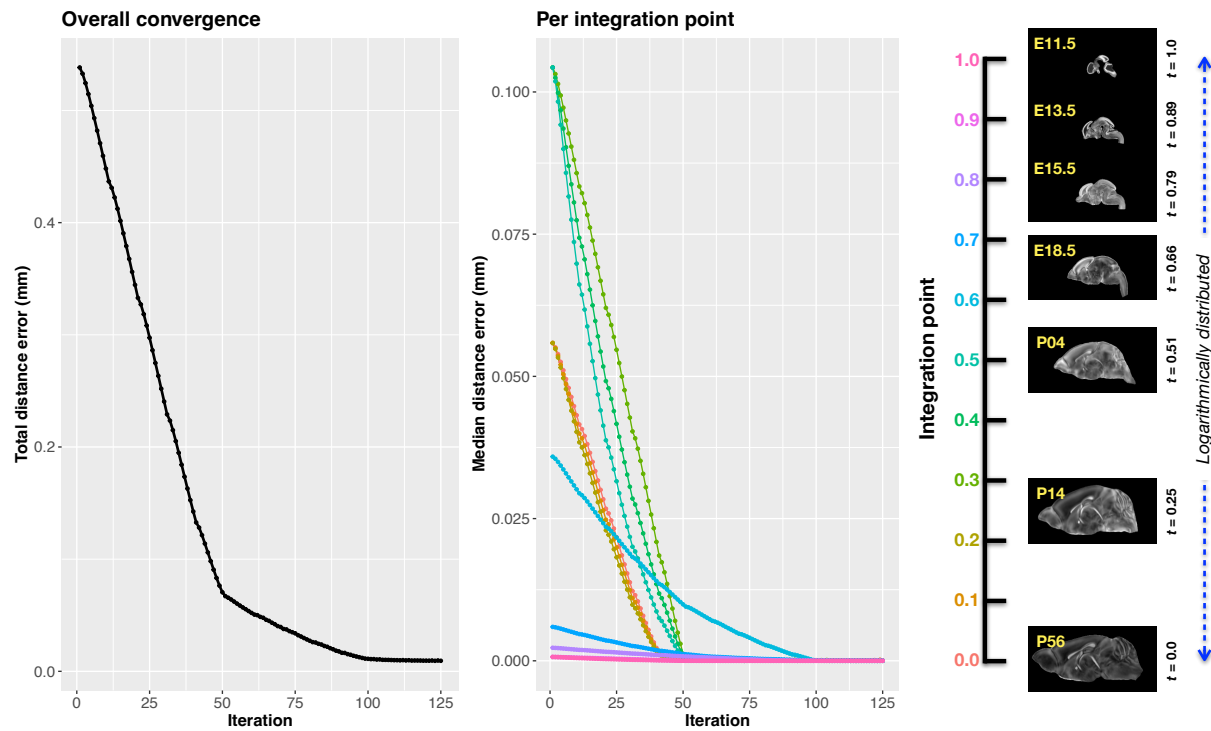


Figure 3: Convergence of the optimization of the velocity field for describing the transformation through the developmental stages from E11.5 through P56.

## 161 Applications

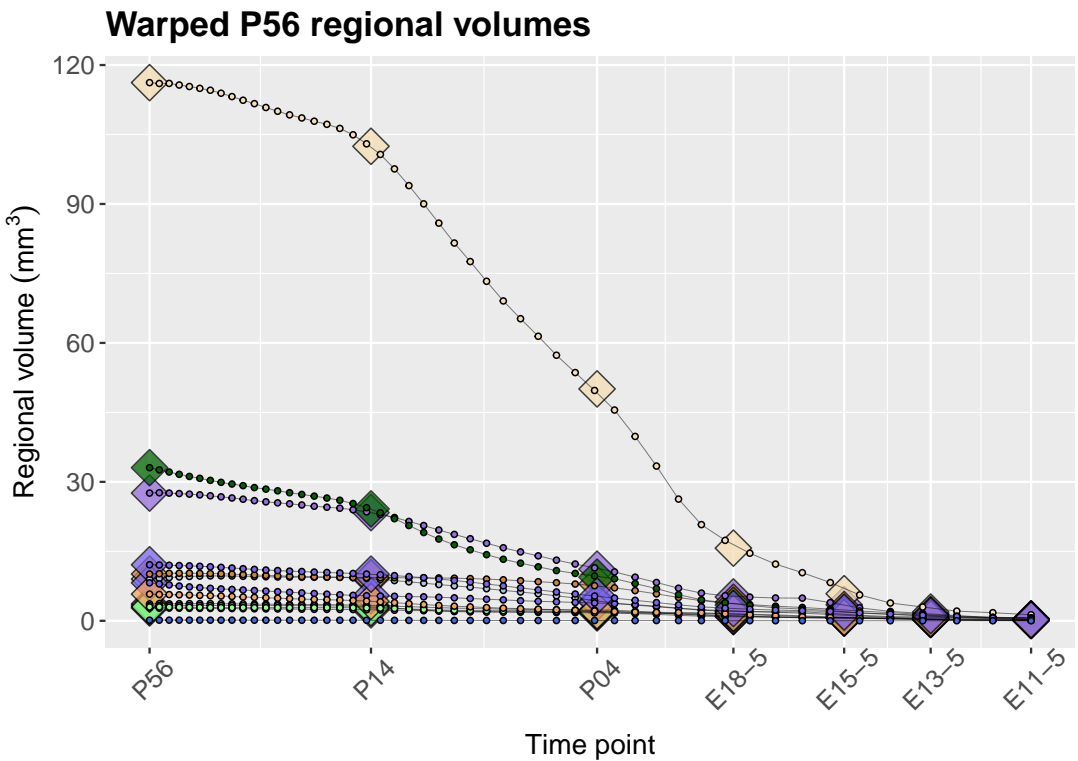


Figure 4: Warped P56.

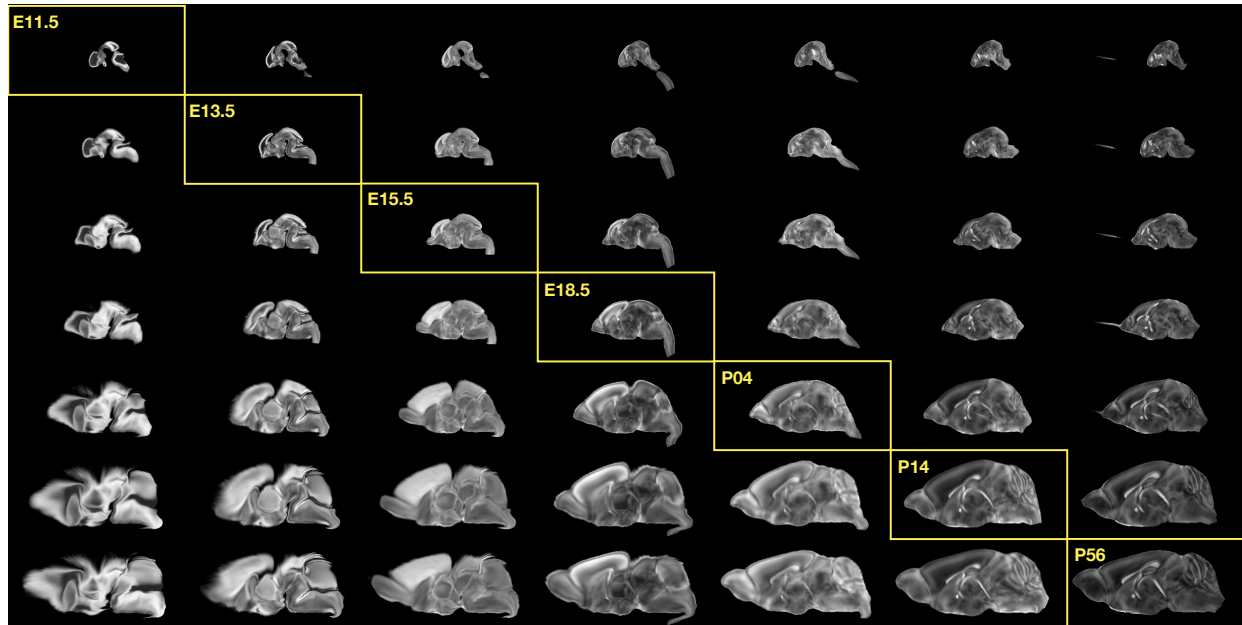


Figure 5: Mid-sagittal visualization of the effects of the transformation model in warping every developmental stage to the time point of every other developmental stage. The original images are located along the diagonal. Columns correspond to the warped original image whereas the rows represent the reference space to which each image is warped.

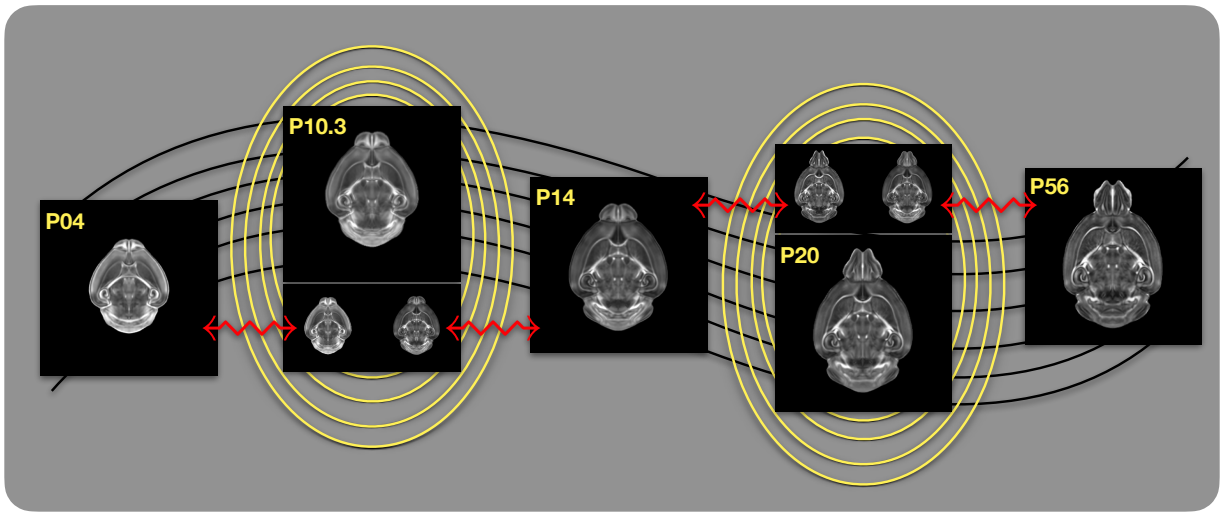


Figure 6: Illustration of the use of the velocity flow model for creating pseudo-templates at continuous time points not represented in one of the existing developmental stages. For example, FA templates at time point P10.3 and P20 can be generated by warping the existing temporally adjacent developmental templates to the target time point and using those images in the ANTsX template building process.

<sub>162</sub> **Methods**

<sub>163</sub> **Preprocessing: bias field correction and denoising**

<sub>164</sub> As in human studies, bias field correction and image denoising are standard preprocessing  
<sub>165</sub> steps in improving overall image quality in mouse brain images. The bias field, a gradual  
<sub>166</sub> spatial intensity variation in images, can arise from various sources such as magnetic field in-  
<sub>167</sub> homogeneity or acquisition artifacts, leading to distortions that can compromise the quality  
<sub>168</sub> of brain images. Correcting for bias fields ensures a more uniform and consistent representa-  
<sub>169</sub> tion of brain structures, enabling accurate quantitative analysis. Additionally, brain images  
<sub>170</sub> are often susceptible to various forms of noise, which can obscure subtle features and affect  
<sub>171</sub> the precision of measurements. Denoising techniques help mitigate the impact of noise, en-  
<sub>172</sub> hancing the signal-to-noise ratio and improving the overall image quality. The well-known  
<sub>173</sub> N4 bias field correction algorithm<sup>24</sup> has its origins in the ANTs toolkit which was imple-  
<sub>174</sub> mented and introduced into the ITK toolkit. Similarly, ANTsX contains an implementation  
<sub>175</sub> of a well-performing patch-based denoising technique<sup>53</sup> and is also available as a image filter  
<sub>176</sub> to the ITK community.

<sub>177</sub> **ANTsXNet mouse brain applications**

<sub>178</sub> *General notes regarding deep learning training.*

<sub>179</sub> All network-based approaches described below were implemented and organized in the  
<sub>180</sub> ANTsXNet libraries comprising Python (ANTsPyNet) and R (ANTsRNet) analogs using the  
<sub>181</sub> Keras/Tensorflow libraries available as open-source in ANTsX GitHub repositories. For the  
<sub>182</sub> various applications, both share the identically trained weights for mutual reproducibility.  
<sub>183</sub> Training data was provided by manual labeling by various co-authors and expanded using  
<sub>184</sub> both intensity-based and shape-based data augmentation techniques.

<sub>185</sub> Intensity-based data augmentation consisted of randomly added noise based on ITK  
<sub>186</sub> functionality, simulated bias fields based on N4 bias field modeling, and histogram  
<sub>187</sub> warping for mimicking well-known MRI intensity nonlinearities.<sup>25,54</sup> These augmentation

188 techniques are available in ANTsXNet (only ANTsPyNet versions are listed): simulated  
189 bias field: `simulate_bias_field(...)`, image noise: `add_noise_to_image(...)`, and  
190 MRI intensity nonlinear characterization: `histogram_warp_image_intensities(...)`.  
191 Shape-based data augmentation used both random linear and nonlinear deformations. This  
192 functionality is also instantiated within ANTsXNet in terms of random spatial warping:  
193 `randomly_transform_image_data(...)`.

194 For all GPU training, we used Python scripts for creating custom batch generators. As such  
195 batch generators tend to be application-specific, we store them in a separate GitHub reposi-  
196 tory for public availability (<https://github.com/ntustison/ANTsXNetTraining>). In terms of  
197 GPU hardware, all training was done on a DGX (GPUs: 4X Tesla V100, system memory:  
198 256 GB LRDIMM DDR4).

199 *Brain extraction.*

200 Similar to human neuroimage processing, brain extraction is a crucial preprocessing step for  
201 accurate brain mapping. Within ANTsXNet, we have created several deep learning networks  
202 for brain extraction for several image modalities (e.g., T1, FLAIR, fractional anisotropy).  
203 Similarly, for the developmental brain atlas work<sup>47</sup> we developed similar functionality for  
204 mouse brains of different modalities and developmental age. All networks use a conventional  
205 2-D U-net architecture<sup>55</sup> and perform prediction in a slice-wise fashion given the limitations of  
206 the acquisition protocols (e.g., missing slices, slice thickness). Currently, coronal and sagittal  
207 networks are available for both E13.5 and E15.5 data and coronal network for T2-weighted  
208 MRI. In ANTsPyNet, this functionality is available in the program `brain_extraction(...)`.  
209 Even when physical brain extraction is performed prior to image acquisition, artifacts, such  
210 as bubbles or debris, can complicate subsequent processing. Similar to the brain extraction  
211 networks, a 2-D U-net architecture<sup>55</sup> was created to separate the background and foreground.

212 *Miscellaneous networks: Super-resolution, cerebellum, and hemispherical masking.*

213 To further enhance the data prior to designing mapping protocols, additional networks were  
214 created. A well-performing deep back projection network<sup>56</sup> was ported to ANTsXNet and  
215 expanded to 3-D for various super-resolution applications,<sup>57</sup> including mouse data. Finally,  
216 features of anatomical significance, namely the cerebellum and hemispherical midline were

217 captured in these data using deep learning networks.

## 218 **Image registration**

### 219 **Intra-slice image registration with missing slice imputation**

220 Volumetric gene expression slice data was collated into 3-D volumes using . . . (ask Jeff).

221 Prior to mapping this volume to the corresponding structural data and, potentially, to the  
222 appropriate template, alignment was improved using deformable registration on contiguous  
223 slices. However, one of the complications associated with these image data was the un-  
224 known number of missing slices, the number of consecutive missing slices, and the different  
225 locations of these missing slices. To handle this missing data problem, we found that data  
226 interpolation using the B-spline approximation algorithm cited earlier<sup>52</sup> (ANTsPy function:  
227 `fit_bspline_object_to_scattered_data(...)`). This provided sufficient data interpo-  
228 lation fidelity to perform continuous slicewise registration. Other possible variants that  
229 were considered but deemed unnecessary was performing more than one iteration cycling  
230 through data interpolation and slicewise alignment. The other possibility was incorporating  
231 the super-resolution technique described earlier. But again, our data did not require these  
232 additional steps.

## 233 **Template generation**

234 ANTsX provides functionality for constructing templates from a set (or multi-modal sets) of  
235 input images as originally described<sup>50</sup> and recently used to create the DevCCF templates.<sup>47</sup>  
236 An initial template estimate is constructed from an existing subject image or a voxelwise  
237 average derived from a rigid pre-alignment of the image population. Pairwise registration  
238 between each subject and the current template estimate is performed using the Symmetric  
239 Normalization (SyN) algorithm.<sup>39</sup> The template estimate is updated by warping all subjects  
240 to the space of the template, performing a voxelwise average, and then performing a “shape  
241 update” of this latter image by warping it by the average inverse deformation, thus yielding

<sup>242</sup> a mean image of the population in terms of both the intensity and shape.

## <sup>243</sup> **Continuous developmental velocity flow transformation model**

<sup>244</sup> Given multiple, linearly or non-linearly ordered point sets where individual points across  
<sup>245</sup> are in one-to-one correspondence, we developed an approach for generating a velocity flow  
<sup>246</sup> transformation model to describe a time-varying diffeomorphic mapping as a variant of the  
<sup>247</sup> inexact landmark matching solution of Joshi and Miller.<sup>48</sup> Integration of the resulting velocity  
<sup>248</sup> field can then be used to describe the displacement between any two time points within this  
<sup>249</sup> time-parameterized domain. Regularization of the sparse correspondence between point sets  
<sup>250</sup> is performed using a generalized B-spline scattered data approximation technique,<sup>52</sup> also  
<sup>251</sup> developed by the ANTsX developers and contributed to ITK.

<sup>252</sup> To apply this methodology to the developmental templates,<sup>47</sup> we coalesced the manual par-  
<sup>253</sup> cellations of the developmental templates into 26 common anatomical regions (13 per hemi-  
<sup>254</sup> sphere). We then used these regions to generate invertible transformations between suc-  
<sup>255</sup> cessive time points. Specifically each label was used to create a pair of single region images  
<sup>256</sup> resulting in 26 pairs of “source” and “target” images. The multiple image pairs were used  
<sup>257</sup> to iteratively estimate a diffeomorphic pairwise transform. Given the seven atlases E11.5,  
<sup>258</sup> E13.5, E15.5, E18.5, P4, P14, and P56, this resulted in 6 sets of transforms between suc-  
<sup>259</sup> cessive time points. Given the relative sizes between atlases, on the order of  $10^6$  points were  
<sup>260</sup> randomly sampled labelwise in the P56 template space and propagated to each successive  
<sup>261</sup> atlas providing the point sets for constructing the velocity flow model. Approximately 200  
<sup>262</sup> iterations resulted in a steady convergence based on the average Euclidean norm between  
<sup>263</sup> transformed point sets. Ten integration points were used and point sets were distributed  
<sup>264</sup> along the temporal dimension using a log transform for a more evenly spaced sampling.  
<sup>265</sup> Further details including links to data and scripts to reproduce our reported results is found  
<sup>266</sup> in the associated GitHub repository.<sup>1</sup>

<sup>267</sup> One potential application is the possible construction of “pseudo”-templates at currently  
<sup>268</sup> non-existing developmental stages.

---

<sup>1</sup><https://github.com/ntustison/MouseBrainVelocityFlow/>

269 **Visualization**

270 To complement the well-known visualization capabilities of R and Python, e.g., `ggplot2`  
271 and `matplotlib`, respectively, image-specific visualization capabilities are available in the  
272 `ants.plot(...)` (Python) and `plot.antsImage(...)` (R). These are capable of illustrating  
273 multiple slices in different orientations with both other image overlays as well as label images.

274 **References**

- 275 1. Keller, P. J. & Ahrens, M. B. Visualizing whole-brain activity and development at  
276 the single-cell level using light-sheet microscopy. *Neuron* **85**, 462–83 (2015).
- 277 2. La Manno, G. *et al.* Molecular architecture of the developing mouse brain. *Nature*  
278 **596**, 92–96 (2021).
- 279 3. Wen, L. *et al.* Single-cell technologies: From research to application. *Innovation*  
280 (*Camb*) **3**, 100342 (2022).
- 281 4. Oh, S. W. *et al.* A mesoscale connectome of the mouse brain. *Nature* **508**, 207–14  
282 (2014).
- 283 5. Gong, H. *et al.* Continuously tracing brain-wide long-distance axonal projections in  
284 mice at a one-micron voxel resolution. *Neuroimage* **74**, 87–98 (2013).
- 285 6. Li, A. *et al.* Micro-optical sectioning tomography to obtain a high-resolution atlas of  
286 the mouse brain. *Science* **330**, 1404–8 (2010).
- 287 7. Ueda, H. R. *et al.* Tissue clearing and its applications in neuroscience. *Nat Rev*  
288 *Neurosci* **21**, 61–79 (2020).
- 289 8. Ståhl, P. L. *et al.* Visualization and analysis of gene expression in tissue sections by  
290 spatial transcriptomics. *Science* **353**, 78–82 (2016).
- 291 9. Burgess, D. J. Spatial transcriptomics coming of age. *Nat Rev Genet* **20**, 317 (2019).
- 292
- 293 10. MacKenzie-Graham, A. *et al.* A multimodal, multidimensional atlas of the C57BL/6J  
294 mouse brain. *J Anat* **204**, 93–102 (2004).
- 295 11. Mackenzie-Graham, A. J. *et al.* Multimodal, multidimensional models of mouse brain.  
296 *Epilepsia* **48 Suppl 4**, 75–81 (2007).
- 297 12. Dong, H. W. *Allen reference atlas. A digital color brain atlas of the C57BL/6J male*  
298 *mouse.* (John Wiley; Sons, 2008).

- 299 13. Wang, Q. *et al.* The allen mouse brain common coordinate framework: A 3D reference  
300 atlas. *Cell* **181**, 936–953.e20 (2020).
- 301 14. Johnson, G. A. *et al.* Waxholm space: An image-based reference for coordinating  
302 mouse brain research. *Neuroimage* **53**, 365–72 (2010).
- 303 15. Oguz, I., Zhang, H., Rumple, A. & Sonka, M. RATS: Rapid automatic tissue segmen-  
304 tation in rodent brain MRI. *J Neurosci Methods* **221**, 175–82 (2014).
- 305 16. Sawiak, S. J., Picq, J.-L. & Dhenain, M. Voxel-based morphometry analyses of in  
306 vivo MRI in the aging mouse lemur primate. *Front Aging Neurosci* **6**, 82 (2014).
- 307 17. Ashburner, J. SPM: A history. *Neuroimage* **62**, 791–800 (2012).
- 308
- 309 18. Modat, M. *et al.* Fast free-form deformation using graphics processing units. *Comput  
310 Methods Programs Biomed* **98**, 278–84 (2010).
- 311 19. Tyson, A. L. *et al.* Accurate determination of marker location within whole-brain  
312 microscopy images. *Sci Rep* **12**, 867 (2022).
- 313 20. Pallast, N. *et al.* Processing pipeline for atlas-based imaging data analysis of struc-  
314 tural and functional mouse brain MRI (AIDAmri). *Front Neuroinform* **13**, 42 (2019).
- 315 21. Jenkinson, M., Beckmann, C. F., Behrens, T. E. J., Woolrich, M. W. & Smith, S. M.  
316 FSL. *Neuroimage* **62**, 782–90 (2012).
- 317 22. Yeh, F.-C., Wedeen, V. J. & Tseng, W.-Y. I. Generalized q-sampling imaging. *IEEE  
318 Trans Med Imaging* **29**, 1626–35 (2010).
- 319 23. Jorge Cardoso, M. *et al.* STEPS: Similarity and truth estimation for propagated  
320 segmentations and its application to hippocampal segmentation and brain parcelation.  
*Med Image Anal* **17**, 671–84 (2013).
- 321 24. Tustison, N. J. *et al.* N4ITK: Improved N3 bias correction. *IEEE Trans Med Imaging*  
322 **29**, 1310–20 (2010).

- 323 25. Tustison, N. J. *et al.* The ANTsX ecosystem for quantitative biological and medical  
324 imaging. *Sci Rep* **11**, 9068 (2021).
- 325 26. Goubran, M. *et al.* Multimodal image registration and connectivity analysis for inte-  
326 gration of connectomic data from microscopy to MRI. *Nat Commun* **10**, 5504 (2019).
- 327 27. Celestine, M., Nadkarni, N. A., Garin, C. M., Bougacha, S. & Dhenain, M. Sammba-  
328 MRI: A library for processing SmAll-MaMmal BrAin MRI data in python. *Front  
Neuroinform* **14**, 24 (2020).
- 329 28. Ioanas, H.-I., Marks, M., Zerbi, V., Yanik, M. F. & Rudin, M. An optimized regis-  
330 tration workflow and standard geometric space for small animal brain imaging. *Neuro-  
image* **241**, 118386 (2021).
- 331 29. Cox, R. W. AFNI: What a long strange trip it's been. *Neuroimage* **62**, 743–7 (2012).  
332
- 333 30. Ni, H. *et al.* A robust image registration interface for large volume brain atlas. *Sci  
334 Rep* **10**, 2139 (2020).
- 335 31. Jin, M. *et al.* SMART: An open-source extension of WholeBrain for intact mouse  
336 brain registration and segmentation. *eNeuro* **9**, (2022).
- 337 32. Fürth, D. *et al.* An interactive framework for whole-brain maps at cellular resolution.  
338 *Nat Neurosci* **21**, 139–149 (2018).
- 339 33. Negwer, M. *et al.* FriendlyClearMap: An optimized toolkit for mouse brain mapping  
340 and analysis. *Gigascience* **12**, (2022).
- 341 34. Klein, S., Staring, M., Murphy, K., Viergever, M. A. & Pluim, J. P. W. Elastix: A  
342 toolbox for intensity-based medical image registration. *IEEE Trans Med Imaging* **29**,  
196–205 (2010).
- 343 35. Carey, H. *et al.* DeepSlice: Rapid fully automatic registration of mouse brain imaging  
344 to a volumetric atlas. *Nat Commun* **14**, 5884 (2023).

- 345 36. Bajcsy, R. & Broit, C. Matching of deformed images. in *Sixth International Conference on Pattern Recognition (ICPR'82)* 351–353 (1982).
- 346
- 347 37. Bajcsy, R. & Kovacic, S. Multiresolution elastic matching. *Computer Vision, Graphics, and Image Processing* **46**, 1–21 (1989).
- 348
- 349 38. Gee, J., Sundaram, T., Hasegawa, I., Uematsu, H. & Hatabu, H. Characterization of regional pulmonary mechanics from serial magnetic resonance imaging data. *Acad Radiol* **10**, 1147–52 (2003).
- 350
- 351 39. Avants, B. B., Epstein, C. L., Grossman, M. & Gee, J. C. Symmetric diffeomorphic image registration with cross-correlation: Evaluating automated labeling of elderly and neurodegenerative brain. *Med Image Anal* **12**, 26–41 (2008).
- 352
- 353 40. Klein, A. *et al.* Evaluation of 14 nonlinear deformation algorithms applied to human brain MRI registration. *Neuroimage* **46**, 786–802 (2009).
- 354
- 355 41. Murphy, K. *et al.* Evaluation of registration methods on thoracic CT: The EMPIRE10 challenge. *IEEE Trans Med Imaging* **30**, 1901–20 (2011).
- 356
- 357 42. Baheti, B. *et al.* The brain tumor sequence registration challenge: Establishing correspondence between pre-operative and follow-up MRI scans of diffuse glioma patients. (2021).
- 358
- 359 43. Wang, H. *et al.* Multi-atlas segmentation with joint label fusion. *IEEE Trans Pattern Anal Mach Intell* **35**, 611–23 (2013).
- 360
- 361 44. Tustison, N. J. *et al.* Optimal symmetric multimodal templates and concatenated random forests for supervised brain tumor segmentation (simplified) with ANTsR. *Neuroinformatics* (2014) doi:[10.1007/s12021-014-9245-2](https://doi.org/10.1007/s12021-014-9245-2).
- 362
- 363 45. Tustison, N. J., Yang, Y. & Salerno, M. Advanced normalization tools for cardiac motion correction. in *Statistical atlases and computational models of the heart - imaging and modelling challenges* (eds. Camara, O. *et al.*) vol. 8896 3–12 (Springer International Publishing, 2015).
- 364

- 365 46. McCormick, M., Liu, X., Jomier, J., Marion, C. & Ibanez, L. ITK: Enabling repro-  
366       ducible research and open science. *Front Neuroinform* **8**, 13 (2014).
- 367 47. Kronman, F. A. *et al.* Developmental mouse brain common coordinate framework.  
368       **bioRxiv** (2023) doi:[10.1101/2023.09.14.557789](https://doi.org/10.1101/2023.09.14.557789).
- 369 48. Joshi, S. C. & Miller, M. I. Landmark matching via large deformation diffeomor-  
370       phisms. *IEEE Trans Image Process* **9**, 1357–70 (2000).
- 371 49. Christensen, G. E., Rabbitt, R. D. & Miller, M. I. Deformable templates using large  
372       deformation kinematics. *IEEE Trans Image Process* **5**, 1435–47 (1996).
- 373 50. Avants, B. B. *et al.* The optimal template effect in hippocampus studies of diseased  
374       populations. *Neuroimage* **49**, 2457–66 (2010).
- 375 51. Tustison, N. J. *et al.* Optimal symmetric multimodal templates and concatenated  
376       random forests for supervised brain tumor segmentation (simplified) with ANTsR.  
*Neuroinformatics* **13**, 209–25 (2015).
- 377 52. Tustison, N. J. & Amini, A. A. Biventricular myocardial strains via nonrigid regis-  
378       tration of anatomical NURBS model [corrected]. *IEEE Trans Med Imaging* **25**, 94–112  
(2006).
- 379 53. Manjón, J. V., Coupé, P., Martí-Bonmatí, L., Collins, D. L. & Robles, M. Adaptive  
380       non-local means denoising of MR images with spatially varying noise levels. *J Magn  
Reson Imaging* **31**, 192–203 (2010).
- 381 54. Nyúl, L. G., Udupa, J. K. & Zhang, X. New variants of a method of MRI scale  
382       standardization. *IEEE Trans Med Imaging* **19**, 143–50 (2000).
- 383 55. Falk, T. *et al.* U-net: Deep learning for cell counting, detection, and morphometry.  
384       *Nat Methods* **16**, 67–70 (2019).
- 385 56. Haris, M., Shakhnarovich, G. & Ukita, N. Deep back-projection networks for super-  
386       resolution. in *2018 IEEE/CVF Conference on Computer Vision and Pattern Recog-  
nition* 1664–1673 (2018). doi:[10.1109/CVPR.2018.00179](https://doi.org/10.1109/CVPR.2018.00179).

- <sup>387</sup> 57. avants, brian *et al.* Concurrent 3D super resolution on intensity and segmentation  
<sup>388</sup> maps improves detection of structural effects in neurodegenerative disease. *medRxiv*  
(2023) doi:[10.1101/2023.02.02.23285376](https://doi.org/10.1101/2023.02.02.23285376).